Journal of Materials Chemistry A

PAPER

View Article Online
View Journal

Cite this: DOI: 10.1039/c7ta00587c

Core/shell-structured hyperbranched aromatic polyamide functionalized graphene nanosheets-poly(*p*-phenylene benzobisoxazole) nanocomposite films with improved dielectric properties and thermostability†

Hao Feng,[a] Wenjun Ma,[a] Zhong-Kai Cui,[b] Xiaoyun Liu,*[a] Jinlou Gu,[a] Shaoliang Lin[a] and Qixin Zhuang*[a]

This study reports the synthesis of core/shell-structured hyperbranched aromatic polyamide functionalized graphene nanosheets-poly(*p*-phenylene benzobisoxazole) (GNs-HAP-PBO) nanocomposite films with improved dielectric properties and thermostability. PBO precursor polymer chains were grafted onto the ample amino-terminated GNs-HAP *via in situ* polymerization, and then the reduction of GNs-HAP and the intramolecular cyclization of PBO precursors were achieved through thermal treatment. The unique core/shell-structure is effective to prevent the aggregation of GNs and improves the dispersion of GNs in the GNs-HAP-PBO nanocomposites, forming microcapacitor networks in the matrix. The GNs-HAP-PBO nanocomposite films exhibit lower dielectric loss in comparison with solvothermally reduced graphene oxide/PBO nanocomposite films. At 1 kHz and 200 °C, a dielectric constant of 66.27 and a dielectric loss of 0.045 are observed in the GNs-HAP-PBO nanocomposite films with 2 wt% GNs-HAP. Moreover, the maximum energy density of the GNs-HAP-PBO nanocomposite films is up to 6 J cm^{-3} owing to the high breakdown strength (132.5 ± 9.3 kV mm^{-1}). The GNs-HAP-PBO nanocomposite films with 2 wt% GNs-HAP also exhibit excellent tensile strength (125 MPa), Young's modulus (6.4 GPa), and high thermal stability (temperature of 5 wt% loss = 643 °C). This work demonstrates a promising strategic approach to fabricating high dielectric materials under extreme environments.

Received 18th January 2017
Accepted 3rd April 2017

DOI: 10.1039/c7ta00587c

rsc.li/materials-a

Introduction

High dielectric constant (high-*k*) polymer nanocomposites have attracted considerable attention in the field of mobile electronic devices, electric vehicles, and electric pulse equipment, owing to the advantages of great flexibility, light weight, low cost, and excellent processability.[1–4] Traditionally, to increase the dielectric constant of polymers, a massive loading content (often over 40 vol%) of high-*k* ceramic fillers such as $BaTiO_3$, TiO_2 and $CaCu_3Ti_4O_{12}$ are introduced into polymers,[5–8] which causes severe damage to the processability and mechanical flexibility of polymer nanocomposites. In contrast, incorporating electrically conductive fillers such as Ag, Ni, carbon nanotubes (CNTs) and graphene nanosheets (GNs) into polymers to form percolated nanocomposites based on percolation theory can dramatically enhance the dielectric constant while maintaining their processability and mechanical flexibility at the percolation threshold (usually <15 vol%) due to the formation of the microcapacitor networks in the polymer matrix.[9–12]

Among these conductive fillers, GNs are promising candidates to enhance the dielectric constant, owing to their unique properties such as high Young's modulus, excellent thermal conductivity, large specific surface area, and in particular high electrical conductivity.[13–15] However, because of the π–π stacking in layers and weak interactions with the polymer matrix, GNs have a strong tendency to stack together. The direct contact between conductive fillers leads to significantly high dielectric loss near the percolation threshold. It may also cause defects or voids in the nanocomposite that can deteriorate both the breakdown strength and the energy storage density. Thus, it is a great challenge to achieve homogeneous and stable dispersion of GNs in a polymer matrix. Recently, several methods have been developed to improve the dispersion of GNs in the polymer matrix. One strategy is to introduce high-*k* and semiconductor ceramic nanoparticles into GNs, which forms more effective

[a]The Key Laboratory of Advanced Polymer Materials of Shanghai, Key Laboratory of Specially Functional Polymeric Materials and Related Technology, Ministry of Education, School of Materials Science and Engineering, East China University of Science and Technology, Shanghai 200237, China. E-mail: qxzhuang@ecust.edu.cn; liuxiaoyun@ecust.edu.cn

[b]Department of Chemistry, Université de Montréal, C.P. 6128, Succ. Centre Ville, Montréal, Québec, H3C 3J7, Canada

† Electronic supplementary information (ESI) available: See DOI: 10.1039/c7ta00587c

microcapacitors and suppresses the formation of conductive pathways.[16,17] Another strategy is to prepare core/shell functionalized GN structures. Poly(*N*-(2-hydroxyphenyl)methacrylamide) grafted GNs, hyperbranched aromatic polyamide functionalized GNs, polyaniline interlayer decorated GNs, and (1-hexadecyl)triphenylphosphonium bromide noncovalently functionalized on the surface of GNs not only ensure good dispersion of GNs in the polymer matrix but also hinder the formation of conductive networks.[18–21]

Meanwhile, most polymer dielectric materials (poly(vinylidene fluoride) (PVDF), polyurethane (PU), biaxially oriented polypropylene (BOPP) *etc.*) exhibit poor stability over a wide range of temperature, due to their low glass transition temperature,[22] which cannot meet the rising demand in applications under extreme conditions such as hybrid and electric vehicles, aerospace power electronics, and underground oil exploration. With light weight, good mechanical strength, and especially excellent thermal stability, poly(*p*-phenylene benzobisoxazole) (PBO) is believed to have wide applications in the dielectric field as a high-temperature resistant polymer matrix.[23–25] Chen *et al.* prepared PBO/graphene nanocomposites with poly(4,6-dihydroxymetaphenylenediamine terephthalamide) modified graphene oxide (PHA-GO) as functional fillers and PBO as the polymer matrix.[26] At 1 kHz and room temperature, the dielectric constant and dielectric loss were 15.8 and 0.45, respectively, below the expected values. The main reason for the unsatisfactory values is that a limited quantity of PBO polymer chains was grafted onto the GNs as a result of insufficient functional groups on the GNs (only a few carboxyl groups located on the edges).

Herein, we provide a novel approach to fabricating core/shell-structured hyperbranched aromatic polyamide functionalized graphene nanosheets-poly(*p*-phenylene benzobisoxazole) (GNs-HAP-PBO) nanocomposite films with outstanding dielectric properties, improved energy storage density, excellent tensile strength and high-temperature resistance. Scheme 1 illustrates the preparation of the GNs-HAP-PBO nanocomposites. In this route, firstly, hyperbranched aromatic polyamide with low conductivity was uniformly attached to the ethylene diamine modified graphene oxide. Then the insulating PBO precursor polymer chains were grafted onto the ample amino-terminated GNs-HAP to form the GNs-HAP-PBO precursor nanocomposites *via in situ* polymerization. At last, the reduction of GNs-HAP and the intramolecular cyclization of PBO precursors were achieved after thermal treatment. Because the reduction procedure occurs in the solid-state nanocomposites, the re-agglomeration of GNs was precluded and the microcapacitor networks form in the matrix. Compared with solvothermally reduced graphene oxide/poly(*p*-phenylene benzobisoxazole) (STRG/PBO) nanocomposites, the GNs-HAP-PBO nanocomposites showed extremely low dielectric loss and high energy storage density due to the interfacial polarization between different layers and confined charge carriers in the shell, indicating that the core/shell-structure was effective to improve the dielectric properties. The GNs-HAP-PBO nanocomposite films are promising dielectric materials to be applied under extreme environments.

Experimental

Materials

Graphite powder (D50 < 500 nm) was purchased from Aladdin Industrial (Shanghai, China). Graphene oxide (GO) was prepared from graphite by a modified Hummers method.[18] 4,6-Di(*tert*-butyldimethylsilylamino)-1,3-di(*tert*-butyldimethylsiloxy) benzene (TBS-DAR) was prepared according to an established method.[27] *N*,*N*-Dimethylformamide (DMF) and *N*-methyl-2-pyrrolidone (NMP) were dried with calcium hydride (CaH_2) prior to distillation. All other reagents were of high purity and used as received.

Preparation of hyperbranched aromatic polyamide functionalized graphene nanosheets (GNs-HAP)

The preparation of GNs-HAP was based on the previous report with some modifications,[28] mainly, the reduction procedure occurring in the solid-state nanocomposites to preclude the

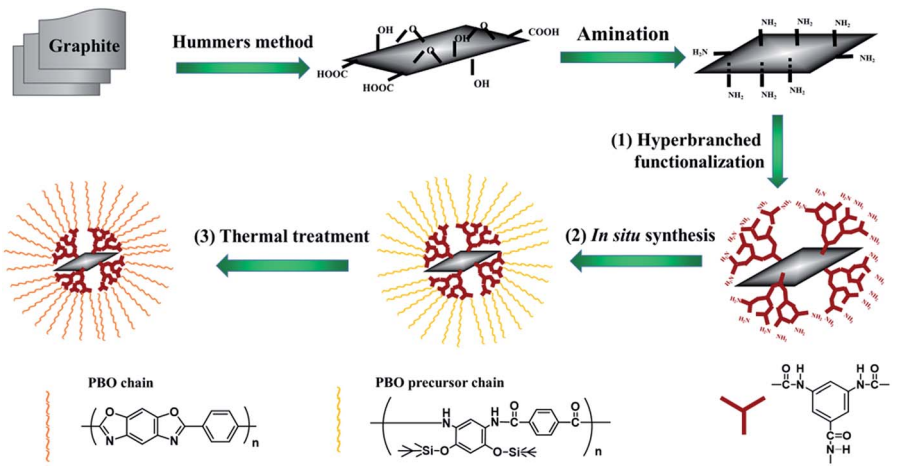

Scheme 1 The overall fabrication procedure for core/shell-structured GNs-HAP-PBO nanocomposites: (1) hyperbranched functionalization, (2) *in situ* synthesis, (3) thermal treatment.

re-agglomeration of GNs. Briefly, GO (200 mg) was dispersed in 100 mL anhydrous DMF under ultrasonication. Then ethylene diamine (EDA, 5 mL), dicyclohexylcarbodiimide (DCC, 0.5 g) and 4-dimethylaminopyridine (DMAP, 0.1 g) were added and the mixture was stirred at 50 °C for 8 h. The mixture was washed with DMF by filtration and dried under vacuum at 40 °C for 12 h to obtain the EDA modified GO (EDA-GO). Subsequently, the EDA-GO was dispersed in 50 mL NMP and 4-dimethylaminopyridine (DMAP, 0.5 g), pyridine (1 mL), triphenyl phosphite (TPP, 2 mL), LiCl (0.1 g) and 3,5-diaminobenzoic acid (3,5-DABA, 3 g) were added, followed by stirring at 100 °C for 10 h. The mixture was washed with DMF to remove the unreacted monomers 3,5-DABA and dried at 40 °C under vacuum for 12 h to obtain hyperbranched aromatic polyamide functionalized graphene nanosheets (GNs-HAP).

Preparation of solvothermally reduced graphene oxide (STRG)

GO (200 mg) was dispersed in 100 mL deionized water under ultrasonication for 1 h and diluted 1 : 1 with 100 mL NMP under ultrasonication for additional 1 h to achieve a stable 1 mg mL^{-1} GO dispersion. Then the dispersion was purged with argon and kept in an oil bath at 240 °C for 24 h under reflux. Finally, the dispersion was filtered and dried at 40 °C under vacuum for 12 h.[29]

Synthesis of GNs-HAP-PBO and STRG/PBO nanocomposite films *via in situ* polymerization

A designated amount of GNs-HAP or STRG was dispersed in anhydrous NMP (5 mL) under ultrasonication for 1 h, leading to a stable suspension. Then TBS-DAR (1.192 g, 2 mmol) was added and the mixture was stirred at 0 °C for 1 h under a nitrogen atmosphere, to which terephthaloyl chloride (0.406 g, 2 mmol) was added and stirred at room temperature for 48 h. The resulting dispersion was cast onto a glass substrate followed by drying at 80 °C under vacuum for 8 h and heat treatment at 300, 350 and 400 °C under a protective argon atmosphere for 1 h, respectively.[30] The film thicknesses varied between 90 and 100 μm. The pure PBO films were synthesized by a similar process in the absence of filler particles.

Characterization

Fourier transform infrared (FTIR) spectra were obtained on a Nicolet 6700 with pressed KBr pellets. Raman spectra were recorded on a Renishaw in Via Reflex Raman spectrometer with a backscattering configuration at 514 nm. X-ray diffraction (XRD) analysis was carried out on a D/MAX 2550 VB/PC rotating anode X-ray multicrystal diffraction spectrometer equipped with a Ni-filtered Cu Kα radiation source and operated at 60 mA and 40 kV. X-ray photoelectron spectroscopy (XPS) was carried out using a Thermo Scientific ESCALAB 250Xi X-ray photoelectron spectrometer equipped with a monochromatic Al Kα X-ray source (1486.6 eV). A high-resolution transmission electron microscope (HRTEM, JEOL JEM-2100) was utilized to obtain detailed morphology and microstructure of GO and GNs-HAP. The fractured surface of the sample was analysed using a field-emission scanning electron microscope (FESEM, Hitachi S-4800). The dielectric properties and the alternating current (ac) electrical properties were analyzed with a Concept 40 Broadband dielectric analyzer (Novocontrol Technologies GmbH & Co. KG, Germany) at 200 °C. Before measurements, the electrodes were painted with a silver paste on both sides of the tablet samples. The dielectric breakdown strength was measured using a CS2674AX ultrahigh hipot tester (Allwin Instrument Co., China) at 200 °C according to the procedure outlined in ASTM D149. Thermogravimetric analyses (TGA) were conducted under a nitrogen gas flow at a heating rate of 10 °C min^{-1}. The mechanical properties of the films were measured using a SANS/CMT4204 mechanical tester with a crosshead speed of 5 mm min^{-1}.

Results and discussion

Dispersions of the GNs-HAP-PBO precursor and STRG/PBO precursor

Fig. 1a shows a photograph of the GNs-HAP-PBO precursor in NMP after an undisturbed period of 24 h. The dispersion of the GNs-HAP-PBO in NMP was significantly improved, and no visible precipitate was observed after 24 h. In contrast, the dispersion of the STRG/PBO precursor was not stable in NMP and the sediment layer of aggregated STRG particles was clearly seen on the bottom of the container (Fig. 1b). By removing the NMP solvent from the glass substrate, the glossy and smooth PBO precursor film (Fig. 1c) and GNs-HAP-PBO precursor nanocomposite film (Fig. 1d) were prepared. Moreover, the dispersion of GNs was uniform and without aggregation in GNs-HAP-PBO precursor nanocomposite film. After converting the PBO precursor into PBO through thermal treatment, a flexible and smooth GNs-HAP-PBO nanocomposite film was obtained (Fig. 1e).

Structural characterization of GNs-HAP-PBO and STRG/PBO nanocomposites

The FTIR spectra of GO, EDA-GO, GNs-HAP, STRG, PBO and GNs-HAP-PBO are shown in Fig. 2a and S1.† For GO, the main

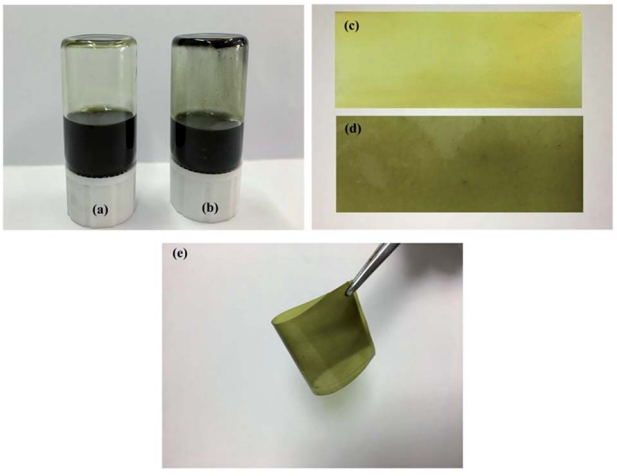

Fig. 1 (a) The GNs-HAP-PBO precursor dispersed in NMP; (b) the STRG/PBO precursor dispersed in NMP; (c) the PBO precursor film; (d) the 2 wt% GNs-HAP-PBO precursor nanocomposite film; (e) the 2 wt% GNs-HAP-PBO nanocomposite film bended by a tweezer.

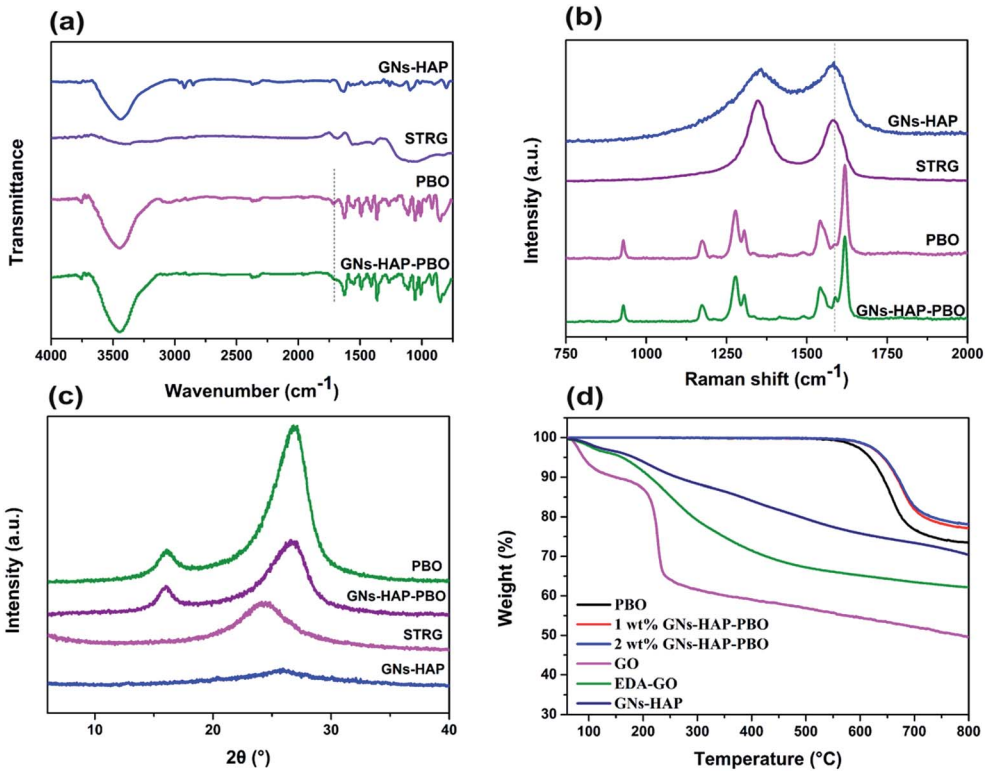

Fig. 2 (a) FTIR spectra, (b) Raman spectra and (c) X-ray diffraction patterns of GNs-HAP, STRG, PBO and GNs-HAP-PBO; (d) TGA curves of GO, EDA-GO, GNs-HAP, PBO and GNs-HAP-PBO.

peaks at around 3412, 1726, 1620, 1224 and 1056 cm^{-1} are attributed to the stretching vibration of O–H, C=O, C=C, –C–O–C–, and C–O, respectively. Compared with GO, the peaks at 2919 and 2851 cm^{-1} are characteristic of the asymmetric and symmetric vibrations of $–CH_2–$ and the peak at 1640 cm^{-1} represents the C=O bond of the amide group in EDA-GO and GNs-HAP, indicating the conversion of carboxyl to amide groups. After solvothermal reduction, the peaks corresponding to C=O at 1726 cm^{-1}, –C–O–C– at 1224 cm^{-1} and C–O at 1056 cm^{-1} disappear in STRG, which suggests that the groups containing oxygen are mostly reduced and the sp^2 networks are restored.[31] As for PBO, the peaks at 1626, 1361 and 1267 cm^{-1} are assigned to the C=N, C–N, and C–O stretching vibration, respectively, corresponding to the characteristic absorption of the oxazole ring. Meanwhile, the characteristic peak at 1718 cm^{-1} is assigned to the stretching vibration of C=O in the terminal carboxylic groups of PBO polymer chains, which diminishes in the spectrum of GNs-HAP-PBO nanocomposites, suggesting the covalent bonding between GNs-HAP and PBO.[32]

To further investigate the interaction between PBO and GNs-HAP, Raman spectroscopy was employed and the spectra are shown in Fig. 2b and S2.† The D peak at 1350 cm^{-1} and G peak at 1600 cm^{-1} in GO are attributed to the optically active in-plane E_{2g} vibration and the defects, respectively, consistent with previous reports.[33] The variation of the D/G intensity ratio suggests a change in the average size of the sp^2 domains. EDA-GO (1.06) and GNs-HAP (0.87) have higher D/G ratios than GO (0.84) indicating that the formation of other defects is caused by the introduction of –CONH– groups on the GNs. Furthermore, the D/G peak ratio (1.29) of STRG is higher than that of GNs-HAP, implying that the oxygen-containing functionalities are removed and more defects are present after reduction. PBO exhibits characteristic peaks at 928, 1180, 1270, 1305, 1544 and 1615 cm^{-1} in the Raman spectrum.[34] A strong fluorescence at 1600 cm^{-1} is observed and the D peak of GNs-HAP at 1350 cm^{-1} is unobvious in the spectrum of GNs-HAP-PBO nanocomposites, which suggests that the amino groups on GNs-HAP participate in polymerization and the covalent bonding between GNs-HAP and PBO mostly forms on the defects of GNs-HAP.

XRD patterns of GO, EDA-GO, GNs-HAP, STRG, PBO and GNs-HAP-PBO are shown in Fig. 2c and S3.† Due to the intercalation of oxygen-containing groups, the XRD pattern of GO exhibits a broad reflection peak (002) at $2\theta = 10.4°$ ($d = 0.84$ nm). For EDA-GO, there are weak and broad peaks at $2\theta = 10.5°$ and $2\theta = 23.5°$, which suggests that groups containing oxygen in GO are mostly removed. After hyperbranched aromatic polyamide functionalization, the peak intensity further decreases and almost no diffraction peaks can be observed. In the XRD pattern of STRG, due to the restacking of the graphene nanosheets during the reduction process, a broad and weak diffraction peak appears at $2\theta = 24.2°$ ($d = 0.37$ nm).[35] The patterns also show the crystalline structure of PBO and GNs-HAP-PBO. The peaks at around $2\theta = 16.2°$ ($d = 0.55$ nm) and $27.2°$ ($d = 0.33$ nm) of PBO are attributed to the "side-by-side" distance on the (200) plane and "face-to-face" distance on the (010) plane between two neighboring polymer chains,

respectively.[36] In GNs-HAP-PBO nanocomposites, the orientation degree of PBO decreases with the loading of GNs-HAP, indicating that GNs-HAP are sufficiently dispersed between the polymer chains during the *in situ* polymerization and hinder the orientation of PBO molecular chains.

Fig. 2d shows the TGA thermograms of GO, EDA-GO, and GNs-HAP. The TGA thermogram of GO includes two stages: first, the weight loss stage starting below 100 °C is attributed to the removal of absorbed water; second, the weight loss at around 200 °C is ascribed to the decomposition of labile oxygen-containing functional groups from the GO layers. For EDA-GO, there is a significant weight loss at around 150 °C, which can be attributed to the pyrolysis of EDA groups and residual functional groups from GO. Compared with EDA-GO, GNs-HAP shows enhanced thermal stability due to the grafting of hyperbranched aromatic polyamide chains. According to a previous report,[37] graphite is stable at 800 °C in nitrogen, so the weight loss of GNs-HAP at 800 °C in nitrogen is attributed to the decomposition of hyperbranched aromatic polyamide attached to GNs. It is calculated that GNs-HAP contain about 30 wt% hyperbranched aromatic polyamide chains and 70 wt% graphene backbone.

The surface chemical states and atomic ratio of each element in GO, GNs-HAP, and GNs-HAP-PBO are analyzed by XPS. GNs-HAP shows an intensified nitrogen peak at 399 eV and decreased oxygen peak at 530 eV compared with that of GO (Fig. 3a).[38] The C : O ratio of GO is 0.67 : 0.33 and the C : O : N ratio of GNs-HAP is 0.72 : 0.16 : 0.12, which demonstrates the de-oxygenation or oxygen substitution by nitrogen. Through fitting them, the characteristic peaks C–O (286.4 eV), C═O (287.6 eV) and O–C═O (288.6 eV) associated with the oxygen element of GO (Fig. 3b) have been obviously reduced, while C–N (285.9 eV) and O═C–N (288 eV) appear in the C 1s XPS of GNs-HAP spectra (Fig. 3c), which confirms the hyperbranched aromatic polyamide functionalization of GNs.[39] The C : O : N ratio of GNs-HAP-PBO is 0.74 : 0.14 : 0.12, close to the theoretical calculation of the elements in the PBO polymer, which is owing to only 2 wt% GNs-HAP in GNs-HAP-PBO nanocomposites. Moreover, the C 1s XPS spectrum of GNs-HAP-PBO (Fig. 3d) shows three different peaks

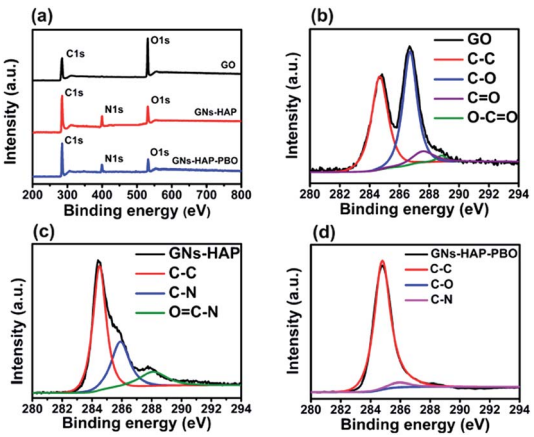

Fig. 3 (a) XPS survey spectra of the GO, GNs-HAP, and GNs-HAP-PBO. C 1s XPS spectra of (b) GO, (c) GNs-HAP and (d) GNs-HAP-PBO.

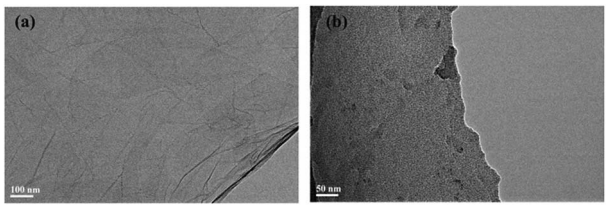

Fig. 4 TEM images of (a) GO, (b) GNs-HAP.

at 284.8, 285.9 and 286.8 eV, corresponding to the C–C, C–N, and C–O bonds in PBO, respectively.

The morphology of GO and GNs-HAP was investigated by TEM. As displayed in Fig. 4a, the surface of the GO sample is relatively smooth. In contrast, the surface of GNs-HAP appears to be rough and clearly covered by the addends, indicating that hyperbranched aromatic polyamide chains are homogeneously grafted onto the surfaces of GNs (Fig. 4b), which is consistent with the XPS results.

Dielectric and energy storage properties of GNs-HAP-PBO and STRG/PBO nanocomposite films

The dielectric constant and dielectric loss of the GNs-HAP-PBO nanocomposites at 200 °C as a function of frequency are shown in Fig. 5a and b. As summarized in Fig. 5c, the dielectric constant increases dramatically as the GNs-HAP content approaches the percolation threshold, according to the percolation theory. The dielectric constant of the nanocomposites with 2 wt% GNs-HAP reaches as high as 66.27, which is 20 times higher than that of the PBO matrix and more than double that of our previous PBO nanocomposites. In addition, the low dielectric loss (0.045, 1 kHz) meets the requirement of high performance dielectric applications. Percolation theory, a typical theory in polymer composites with conductive fillers, can be employed to explain this phenomenon.[40] The relationship between the dielectric constant and the volume fraction of the conductive fillers in the nanocomposites near the percolation threshold can be described by eqn (1) as follows:

$$\varepsilon \propto (f_c - f_{\text{GNs-HAP}})^{-s} \text{ for } f_{\text{GNs-HAP}} < f_c \quad (1)$$

where ε is the dielectric constant of the nanocomposites, f_c is the critical volume fraction at the percolation threshold, $f_{\text{GNs-HAP}}$ is the volume fraction of the GNs-HAP fillers, and s is the critical exponent. For simplification, a mass fraction is used to replace the volume fraction f, and the derived eqn (2) is given below.

$$\varepsilon \propto (m_c - m_{\text{GNs-HAP}})^{-s} \text{ for } m_{\text{GNs-HAP}} < m_c \quad (2)$$

where m_c is the critical mass fraction at the percolation threshold and $m_{\text{GNs-HAP}}$ is the mass fraction of the GNs-HAP fillers. Furthermore, the experimental values of the dielectric constant agree well with eqn (2), with $m_c = 0.022$ and $s = 1.15$. At the percolation threshold content, the conductive core GNs are wrapped by low conductive shell HAP and insulating PBO.[41] In this situation, GNs could nearly link to each other but remain

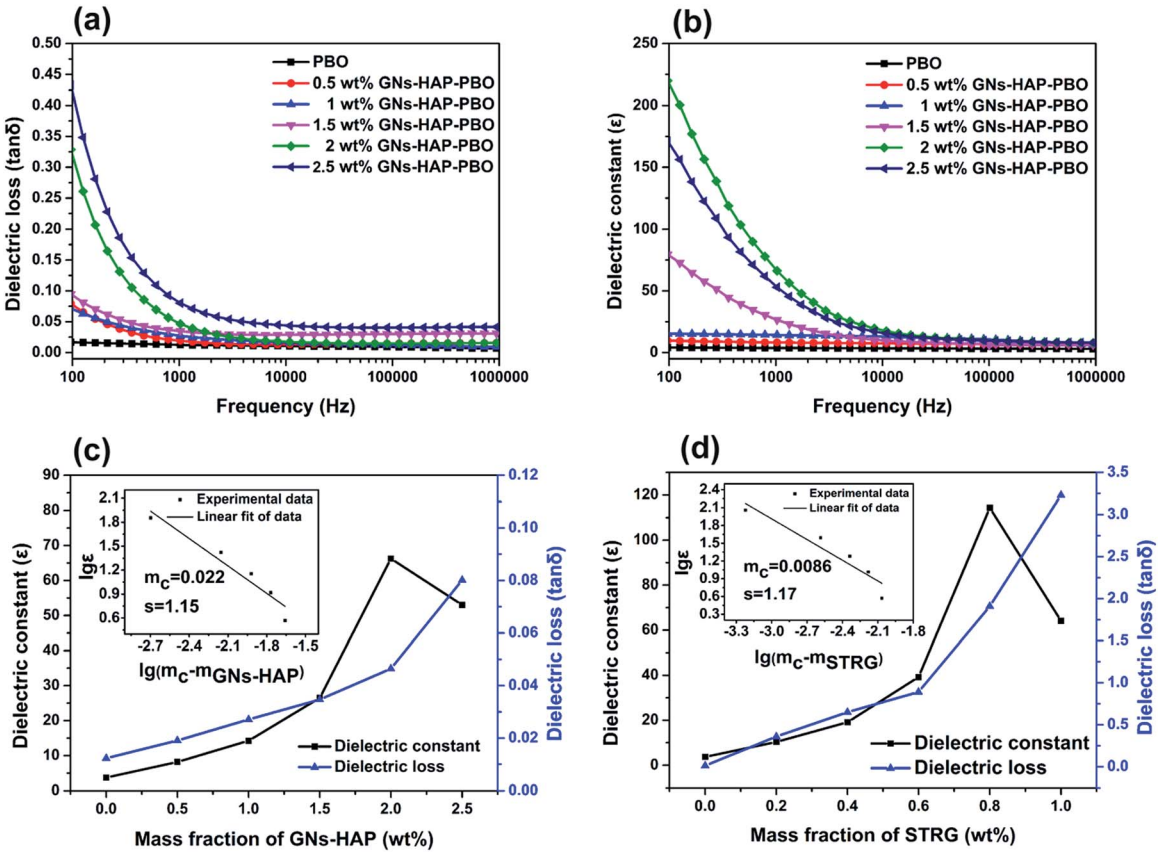

Fig. 5 The frequency dependent dielectric constant (a) and dielectric loss (b) of PBO and the GNs-HAP-PBO nanocomposites at 200 °C; 1 kHz dielectric constant and dielectric loss of the GNs-HAP-PBO nanocomposites (c) and STRG/PBO nanocomposites (d) at 200 °C.

isolated and electrically insulated. When an electric field is applied, migrating electron carriers of the long-range conjugated structure of GNs appear on the internal interfaces through the large π orbital. Moreover, it can be well explained by the microcapacitor theory.[42–44] With the increasing content of GNs-HAP, once the mass fraction reaches the percolation threshold m_c where the GNs-HAP are close to each other, the dielectric constant of the nanocomposites undergoes a sharp increase. This can be attributed to the formation of a large number of microcapacitors and increase in the capacitance of each microcapacitor. As the GNs-HAP content reaches 2.5 wt%, the percolation networks break and conductive networks form. Meanwhile, the dielectric constant decreases and the dielectric loss considerably increases because of the leakage current in the nanocomposites. In contrast, at 1 kHz and 200 °C, the dielectric constant of STRG/PBO nanocomposites (Fig. 5d) is 114.35 at a low filling content of 0.8 wt%, owing to the outstanding conductivity of STRG. The functional groups on the graphene backbone have been completely removed through the solvothermal reduction. However, a dramatic increase of the dielectric constant of STRG/PBO nanocomposites appears with a high dielectric loss of 1.91, as a result of the establishment of the tunneling percolative networks constructed by a certain content of aggregated conductive fillers.

Fig. S4† shows the frequency dependence of ac conductivity for PBO and GNs-HAP-PBO nanocomposite films with the increase of filler contents. With low content of GNs-HAP, the conductivity of the nanocomposites increases with the increasing frequency. When the concentration is 2 wt%, the conductivity of the nanocomposite film is only 10^{-9} S cm^{-1} at 1 kHz and 200 °C. The result confirms that no conducting network was formed, which is consistent with the result of dielectric loss. In this case, the increase in conductivity can be attributed to the decreasing distance between GNs-HAP-PBO. When the concentration is higher than the percolation threshold (2.2 wt%), the conductivity values are almost independent of frequency resulting from the formation of a conductive network.

Table 1 compares the dielectric properties of state-of-the-art graphene based nanocomposites with high temperature resistance at 1 kHz reported in previous literature. The graphene based nanocomposites with high temperature resistance can meet the requirements of the application in processability, flexibility, and working environments. Due to the limitations of the experimental techniques, the dielectric properties of nanocomposites used to be analyzed at room temperature in previous literature. However, the dielectric properties of materials are temperature dependent. The testing temperature for the dielectric properties of dielectric materials should be

Table 1 Dielectric properties of state-of-the-art graphene based nanocomposites with high temperature resistance at 1 kHz

Types of filler material	Matrix	Filler content	Dielectric constant	Dielectric loss	Testing temperature (°C)	Ref.
GNs-HAP	PBO	2 wt%	66.27	0.045	200	This work
STRG	PBO	0.8 wt%	114.35	1.91	200	This work
RGO	PBO	4 wt%	15.8	0.45	25	26 (2013)
RGO-P(o-HPMMA)	P(2-IBO)	1.5 wt%	8.35	0.11	25	18 (2015)
PPD-CFGO	PI	4 wt%	36.9	0.0075	25	48 (2015)
STRG	PI	0.7 wt%	50	1	200	31 (2015)
$BaTiO_3$@RGO	PI	20 vol%	120	0.65	25	45 (2016)

determined according to the realistic working temperature, which is more scientific and accurate. So we analyzed the dielectric properties of GNs-HAP-PBO nanocomposites at 200 °C. Among all the nanocomposites listed in Table 1, the GNs-HAP-PBO nanocomposites showed the best dielectric properties (dielectric constant reached 66.27 and dielectric loss was 0.045) due to the interfacial polarization between different layers and confined charge carriers in the shell, indicating that the core/shell-structure was effective to improve the dielectric properties. For other graphene based nanocomposites with high temperature resistance reported in previous literature, it is difficult to obtain both high dielectric constant and low dielectric loss simultaneously *via* the blend of simply modified GNs and polymer.

Besides dielectric constant, electrical breakdown strength is another important parameter to characterize the energy storage capability of dielectric materials. For simple linear response dielectric materials, the maximum energy density is defined as:

$$U_e = \frac{1}{2}DE = \frac{1}{2}\varepsilon_r\varepsilon_0 E^2 \quad (3)$$

where ε_r is the relative dielectric constant, E is the dielectric breakdown strength, and ε_0 is the vacuum permittivity (8.85×10^{-12} F m^{-1}). The breakdown strength of the GNs-HAP-PBO nanocomposite films is investigated at 200 °C and the error bars are shown as vertical lines (Fig. 6). Under our experimental conditions, the characteristic breakdown strength of PBO is found to be 240 kV mm^{-1}. With the addition of GNs-HAP, the breakdown strength of nanocomposites displays a sharp decrease at a low loading (0.5 wt%), and a gradual decrease with an increasing loading amount. Overall, the breakdown strength of all the investigated GNs-HAP-PBO nanocomposite films below the percolation threshold remains at a high level above 130 kV mm^{-1}. The high breakdown strength of nanocomposites can also be interpreted by the core/shell-structure of GNs-HAP-PBO. Due to the good compatibility and dispersion of GNs-HAP, defect quantities or sizes can be reduced to improve the breakdown strength. For the STRG/PBO nanocomposites, the breakdown strength quickly drops with increasing STRG contents over the entire filler fraction range, which is caused by the STRG conductive networks in the matrix. The 2 wt% GNs-HAP-PBO nanocomposite films (Fig. 6a) exhibit a maximum energy density up to 6 J cm^{-3}, which is about 3.5-fold higher than that of 0.6 wt% STRG/PBO nanocomposite films (Fig. 6b). Currently, polymer film capacitors have energy densities of ~3–10 J cm^{-3} or less and can only be used at temperatures below 105 °C.[46,47] So GNs-HAP-PBO nanocomposite films are expected to be used for various applications including electric vehicles and aerospace power electronics under extreme conditions.

SEM images of the fractured surfaces of PBO and 2 wt% GNs-HAP-PBO nanocomposite films (Fig. 7) also prove the excellent dispersion of GNs-HAP. The cross-section image of the GNs-HAP-PBO nanocomposite films displays homogeneous layered features (pointed by red arrows), which are absent in the image

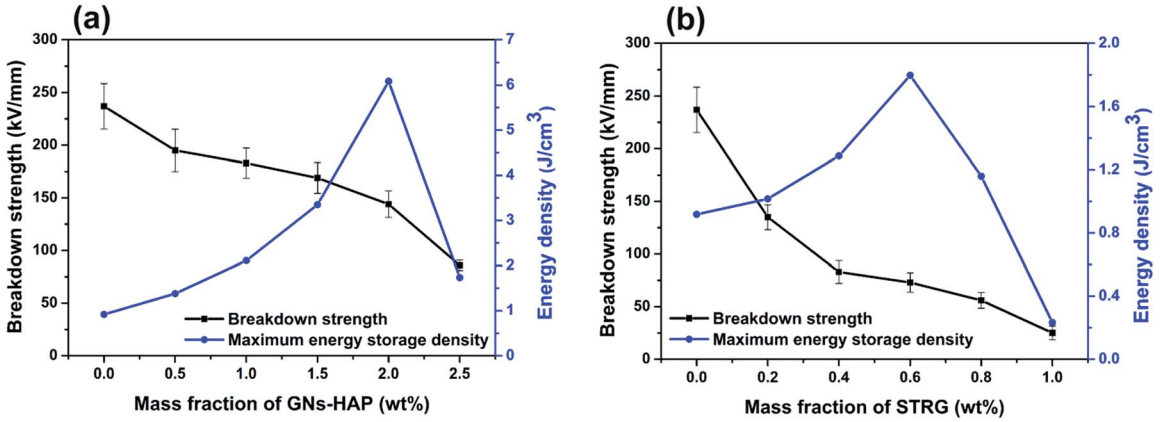

Fig. 6 Breakdown strength and maximum energy storage density of the GNs-HAP-PBO nanocomposites (a) and STRG/PBO nanocomposites (b) as a function of the mass fraction of filler content.

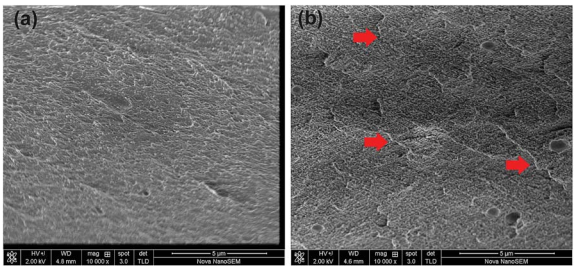

Fig. 7 SEM micrographs of the fractured structure of (a) PBO, (b) 2 wt% GNs-HAP-PBO nanocomposite films.

of PBO. The phenomenon also supports the existence of strong covalently bonding interactions between GNs-HAP and PBO.

Thermal and mechanical properties of PBO and GNs-HAP-PBO nanocomposite films

As demonstrated in the TGA thermograms shown in Fig. 2d, both PBO and GNs-HAP-PBO nanocomposites exhibit outstanding thermal stability under nitrogen below the temperature of 500 °C. Meanwhile, the 5% weight loss temperature of 2 wt% GNs-HAP-PBO shifts toward higher temperature (643 °C) compared with that of PBO. The thermal decomposition trend suggests that *in situ* GNs-HAP-PBO nanocomposites possess better thermal stability than PBO attributed to the covalent bonds between GNs-HAP and PBO molecular chains. With improved compatibility, the heat can be timely transmitted into the nanocomposites by the homogeneously dispersed GNs-HAP.[48] Moreover, the residual weight at 800 °C increased slightly with increasing content of GNs-HAP.

The stress–strain curves of PBO and GNs-HAP-PBO nanocomposite films are shown in Fig. 8 and the tensile properties are summarized in Table 2, demonstrating that the GNs-HAP-PBO nanocomposite films exhibit superior mechanical properties compared with PBO films. The tensile strength and tensile modulus of PBO are 56 MPa and 3.1 GPa, respectively, which are close to those of PBO films prepared from methanesulfonic acid

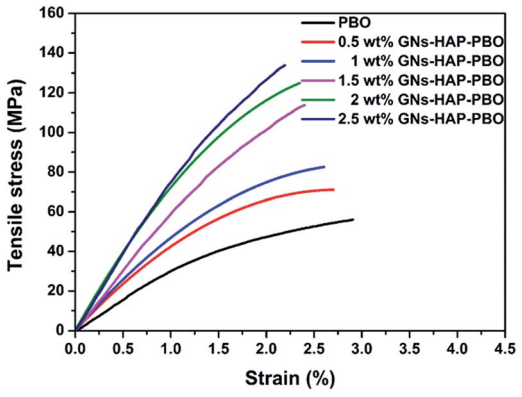

Fig. 8 Stress–strain curves of PBO and GNs-HAP-PBO nanocomposite films with various amounts of GNs-HAP.

Table 2 Summary of mechanical properties of PBO and GNs-HAP-PBO nanocomposite films with various amounts of GNs-HAP

Sample	Tensile strength/ MPa	Young's modulus/ GPa	Elongation (%)
PBO	56.2 ± 4.7	3.1 ± 0.3	2.9 ± 0.3
0.5 wt% GNs-HAP-PBO	71.5 ± 5.3	4.6 ± 0.5	2.7 ± 0.3
1 wt% GNs-HAP-PBO	82.3 ± 5.7	5.2 ± 0.5	2.6 ± 0.4
1.5 wt% GNs-HAP-PBO	113.1 ± 6.5	5.9 ± 0.7	2.4 ± 0.2
2 wt% GNs-HAP-PBO	125.3 ± 7.3	6.4 ± 1.0	2.3 ± 0.3
2.5 wt% GNs-HAP-PBO	133.2 ± 8.1	6.8 ± 0.9	2.2 ± 0.2

solution (tensile strength and tensile modulus are 68.0 MPa and 3.6 GPa, respectively).[49] As shown in Table 1, the tensile strength and tensile modulus of 2 wt% GNs-HAP-PBO increase to 125 MPa (about 123% greater than that of PBO films) and 6.4 GPa, respectively. In contrast, the tensile strength of the STRG/PBO nanocomposite films containing 0.07 vol% STRG is only 67.8 MPa.[44] The ample amino terminals on GNs-HAP react with the PBO monomer *via in situ* polymerization, resulting in improved compatibility of GNs and PBO. The covalent bonds between the GNs-HAP and PBO enhance the interface interactions and restrict the slip of PBO chains, attributed to the formation of the framework in GNs-HAP-PBO nanocomposites.[50] When external forces are applied on the nanocomposites, the strong interface interactions transfer the mechanical load between GNs-HAP and PBO. As a result, the good dispersion of GNs-HAP and the interface interactions from the covalent bond are expected to confer the nanocomposites with excellent tensile strength and thermal properties.

Conclusions

We have demonstrated an effective approach *via in situ* polymerization to preparing core/shell-structured GNs-HAP-PBO nanocomposite films with improved dielectric properties and thermostability. The GNs-HAP-PBO nanocomposite films achieve low dielectric loss and improved energy storage density in comparison with STRG/PBO nanocomposite films, due to the isolation effect of HAP and PBO on GNs, which not only improves the dispersion of fillers in the polymer matrix but also hinders the direct electrical contact. For instance, the dielectric properties of GNs-HAP-PBO nanocomposites exhibit a typical percolation transition near 2.2 wt%. At 1 kHz and 200 °C, the dielectric constant of the nanocomposites with 2 wt% GNs-HAP reaches 66.27 with ultralow dielectric loss (0.045) and high breakdown strength (132.5 ± 9.3 kV mm^{-1}). In addition, the tensile strength and tensile modulus increase to 125 MPa and 6.4 GPa, respectively. Meanwhile, the nanocomposites are thermally stable below 500 °C as revealed by TGA. The improved dielectric properties, energy storage density, heat-resistance and tensile strength make the GNs-HAP-PBO nanocomposite films more suitable for high-temperature and high dielectric applications.

Acknowledgements

This work was financially supported by the National Natural Science Foundation of China (51573045), the International Collaboration Research Program of Science and Technology Commission of Shanghai (16520722000) and the Key Laboratory of Advanced Polymer Materials of Shanghai (Grant No. ZD20150202).

Notes and references

1 Z. M. Dang, J. K. Yuan, S. H. Yao and R. J. Liao, *Adv. Mater.*, 2013, **25**, 6334–6365.
2 Q. Li, L. Chen, M. R. Gadinski, S. Zhang, G. Zhang, H. Li, A. Haque, L. Q. Chen, T. Jackson and Q. Wang, *Nature*, 2015, **523**, 576–579.
3 X. Huang and P. Jiang, *Adv. Mater.*, 2015, **27**, 546–554.
4 M. Q. Le, J. F. Capsal, J. Galineau, F. Ganet, X. Yin, M. D. Yang, J. F. Chateaux, L. Renaud, C. Malhaire, P. J. Cottinet and R. Liang, *Sci. Rep.*, 2015, **5**, 11814.
5 H. Tang, Y. Lin and H. A. Sodano, *Adv. Energy Mater.*, 2012, **2**, 469–476.
6 L. Liu, Y. Zhang, F. Lv, W. Tong, L. Ding, P. K. Chu and P. Li, *RSC Adv.*, 2016, **6**, 86817–86823.
7 S. Liu and J. Zhai, *J. Mater. Chem. A*, 2015, **3**, 1511–1517.
8 Q. G. Chi, J. F. Dong, C. H. Zhang, C. P. Wong, X. Wang and Q. Q. Lei, *J. Mater. Chem. C*, 2016, **4**, 8179–8188.
9 Z. M. Dang, M. S. Zheng and J. W. Zha, *Small*, 2016, **12**, 1688–1701.
10 Q. Zhuang, X. Mao, Z. Xie, X. Liu, Q. Wang, Y. Chen and Z. Han, *J. Polym. Sci., Part A: Polym. Chem.*, 2012, **50**, 4732–4739.
11 Y. Shen, Y. Lin, M. Li and C. W. Nan, *Adv. Mater.*, 2007, **19**, 1418–1422.
12 X. Peng, W. Xu, L. Chen, Y. Ding, S. Chen, X. Wang and H. Hou, *J. Mater. Chem. C*, 2016, **4**, 6452–6456.
13 F. Bonaccorso, L. Colombo, G. Yu, M. Stoller, V. Tozzini, A. C. Ferrari, R. S. Ruoff and V. Pellegrini, *Science*, 2015, **347**, 1246501.
14 R. Raccichini, A. Varzi, S. Passerini and B. Scrosati, *Nat. Mater.*, 2015, **14**, 271–279.
15 B. Luo and L. J. Zhi, *Energy Environ. Sci.*, 2015, **8**, 456–477.
16 D. Wang, T. Zhou, J. W. Zha, J. Zhao, C. Y. Shi and Z. M. Dang, *J. Mater. Chem. A*, 2013, **1**, 6162–6168.
17 X. J. Zhang, G. S. Wang, Y. Z. Wei, L. Guo and M. S. Cao, *JJ. Mater. Chem. A*, 2013, **1**, 12115–12122.
18 Y. Chen, S. Zhang, X. Liu, Q. Pei, J. Qian, Q. Zhuang and Z. Han, *Macromolecules*, 2015, **48**, 365–372.
19 J. Shang, Y. Zhang, L. Yu, X. Luan, B. Shen, Z. Zhang, F. Lv and P. K. Chu, *J. Mater. Chem. A*, 2013, **1**, 884–890.
20 J. Wang, J. Wu, W. Xu, Q. Zhang and Q. Fu, *Compos. Sci. Technol.*, 2014, **91**, 1–7.
21 C. Wu, X. Huang, G. Wang, X. Wu, K. Yang, S. Li and P. Jiang, *J. Mater. Chem.*, 2012, **22**, 7010–7019.
22 J. M. Adhikari, M. R. Gadinski, Q. Li, K. G. Sun, M. A. Reyes-Martinez, E. Iagodkine, A. L. Briseno, T. N. Jackson, Q. Wang and E. D. Gomez, *Adv. Mater.*, 2016, **28**, 10095–10102.
23 Y. Chen, X. Liu, X. Mao, Q. Zhuang, Z. Xie and Z. Han, *Nanoscale*, 2014, **6**, 6440–6447.
24 J. Wei, S. Zhang, X. Liu, J. Qian, J. Hua, X. Li and Q. Zhuang, *J. Mater. Chem. A*, 2015, **3**, 8205–8214.
25 M. J. Lee, J. K. Hwang, J. H. Kim, H. S. Lim, Y. K. Sun, K. D. Suh and Y. M. Lee, *J. Power Sources*, 2016, **305**, 259–266.
26 Y. Chen, Q. Zhuang, X. Liu, J. Liu, S. Lin and Z. Han, *Nanotechnology*, 2013, **24**, 245702.
27 T. Fukumaru, T. Fujigaya and N. Nakashima, *Macromolecules*, 2012, **45**, 4247–4253.
28 T. Chen, J. Qiu, K. Zhu, J. Li, J. Wang, S. Li and X. Wang, *J. Phys. Chem. B*, 2015, **119**, 4521–4530.
29 S. Dubin, S. Gilje, K. Wang, V. C. Tung, K. Cha, A. S. Hall, J. Farrar, R. Varshneya, Y. Yang and R. B. Kaner, *ACS Nano*, 2010, **4**, 3845–3852.
30 S. Luo, J. Liu, H. Lin, B. A. Kazanowska, M. D. Hunckler, R. K. Roeder and R. Guo, *J. Mater. Chem. A*, 2016, **4**, 17050–17062.
31 P. Zhang, J. He, Z.-K. Cui, X. Li, X. Liu, S. Zhang, Q. Zhuang and Z. Han, *Polymer*, 2015, **65**, 262–269.
32 Z. Hu, N. Li, J. Li, C. Zhang, Y. Song, X. Li, G. Wu, F. Xie and Y. Huang, *Polymer*, 2015, **71**, 8–14.
33 L. Huang, P. Zhu, G. Li, D. Lu, R. Sun and C. Wong, *J. Mater. Chem. A*, 2014, **2**, 18246–18255.
34 Q. Zhuang, X. Liu, Q. Wang, X. Liu, J. Zhou and Z. Han, *J. Mater. Chem.*, 2012, **22**, 12381–12388.
35 W. Zhao, J. Kong, H. Liu, Q. Zhuang, J. Gu and Z. Guo, *Nanoscale*, 2016, **8**, 19984–19993.
36 T. Fukumaru, T. Fujigaya and N. Nakashima, *Polym. Chem.*, 2012, **3**, 369–376.
37 Y. Liu, R. J. Deng, Z. Wang and H. T. Liu, *J. Mater. Chem.*, 2012, **22**, 13619–13624.
38 X. Mei and J. Ouyang, *Carbon*, 2011, **49**, 5389–5397.
39 M. Li, X. Huang, C. Wu, H. Xu, P. Jiang and T. Tanaka, *J. Mater. Chem.*, 2012, **22**, 23477–23484.
40 C. W. Nan, Y. Shen and J. Ma, *Annu. Rev. Mater. Res.*, 2010, **40**, 131–151.
41 L. Y. Xie, X. Y. Huang, Y. H. Huang, K. Yang and P. K. Jiang, *J. Phys. Chem. C*, 2013, **117**, 22525–22537.
42 Q. Li, Q. Z. Xue, L. Z. Hao, X. L. Gao and Q. B. Zheng, *Compos. Sci. Technol.*, 2008, **68**, 2290–2296.
43 C. Wu, X. Y. Huang, X. F. Wu, L. Y. Xie, K. Yang and P. K. Jiang, *Nanoscale*, 2013, **5**, 3847–3855.
44 Q. K. Guo, Q. Z. Xue, J. Sun, M. D. Dong, F. J. Xia and Z. Y. Zhang, *Nanoscale*, 2015, **7**, 3660–3667.
45 L. Liu, Y. Zhang, F. Lv, W. Tong, L. Ding, P. K. Chu and P. Li, *RSC Adv.*, 2016, **6**, 86817–86823.
46 C. Yang, Y. H. Lin and C. W. Nan, *Carbon*, 2009, **47**, 1096–1101.
47 X. Y. Huo, W. P. Li, J. J. Zhu, L. L. Li, Y. Li, L. H. Luo and Y. J. Zhu, *J. Phys. Chem. C*, 2015, **119**, 25786–25791.
48 X. Fang, X. Liu, Z.-K. Cui, J. Qian, J. Pan, X. Li and Q. Zhuang, *J. Mater. Chem. A*, 2015, **3**, 10005–10012.
49 C. Zhou, S. Wang, Q. Zhuang and Z. Han, *Carbon*, 2008, **46**, 1232–1240.
50 Y. Li, Q. Duan, Y. Li, Z. Hu, J. Li, Y. Song and Y. Huang, *RSC Adv.*, 2016, **6**, 86245–86252.